Measurements of the Three Dimensional Structure of Flames at Low Turbulence

M.R. Harker, T. Hattrell, M. Lawes, C.G.W. Sheppard, N. Tripathi and R. Woolley

School of Mechanical Engineering, University of Leeds

Leeds, United Kingdom

Abstract

The development of spark ignited flame kernels in a turbulent field is strongly dependent upon the nature of the three dimensional (3-D) turbulence adjacent to the ignition source. The turbulence scales vary in 3-D from shot to shot, resulting in successive flame kernels developing differently and thereby causing cyclic variations in, for example, spark ignition engines. It is necessary to quantify the scales affecting the flame at any instant for the accurate measurement of burn rate of such flame kernels, which requires visualization of the flame surface in 3-D. The experiments reported here employ a multiple sheet mie-scattered light technique to successfully characterize a non-stabilized expanding turbulent flame kernel in 3-D. A novel algorithm was developed to construct the flame surface in 3-D which enabled accurate calculation of parameters such as flame surface density, reaction progress variables and turbulent flame thickness.

Keywords : Turbulent, Premixed, Three dimensional, Laser sheet, Experimental

Correspondence to : Navanshu Tripathi (mnnt@leeds.ac.uk)

1. Introduction

Spark ignited flame kernels in a turbulent field do not immediately experience the full spectrum of turbulence scales present; initially they are wrinkled only by scales of smaller dimensions than the kernel, larger scales merely convecting them. Under nominally identical

mean turbulence conditions, successive flame kernels behave differently; dependent upon the nature of the three dimensional (3-D) eddies adjacent to the ignition source, and thereafter encountered by the growing flame, from event to event. Not until the kernel becomes large enough to encompass the bulk of scales available in the turbulent field does the burn rate becomes consistent from shot to shot (Abdel-Gayed et al., 1987). This is possibly the principal cause of cyclic variability in spark ignition engines (Aleiferis et al., 2004; Vermorel et al., 2009) and ignition variability in gas turbines (Lefebvre, 1999). Slow burning mixtures are particularly affected and the phenomenon is an obstacle to the development of low emissions lean burn and high exhaust gas recirculation engines.

By their inherent nature, turbulent flames are thicker, highly wrinkled, curved and stretched. The structure of a turbulent flame is a rewarding concept for study because it can have a direct effect on the burning rate. The burning rate of such flames is often expressed in terms of a turbulent burning velocity (u_t), a parameter used in many thermodynamic cycle models of engine combustion and in explosion hazard assessment. The value of u_t depends upon the amount of wrinkling of the flame's surface and its effect on the total surface area available for reaction (Bradley et al., 2011; Lipatnikov and Chomiak, 2002). In order to quantify the effect of wrinkling on a flame's structure, there are several parameters of interest, for example; flame surface density (FSD) denoted by $\sum$ (Halter et al., 2009), which is the area of flame surface per unit volume of flame; reaction progress variable (RPV) denoted by c (Bray et al., 2005), a parameter to assess the transition from unburned reactants to burned products through the flame; and statistics of flame curvature (Chakraborty et al., 2008), used to investigate the complexity of wrinkling of the flame's surface. However, measurement of u_t is problematic; particularly for flame kernels in their early stages of development, where it is necessary to quantify the turbulent scales affecting the flame at any instant and where these scales vary in 3-D and from explosion to explosion.

Turbulent flames have been routinely observed using (2-D) sheet imaging techniques, this is especially effective in turbulent systems where it is possible to characterize the flame wrinkling (Hicks et al., 1994), flame curvature (Lee et al., 1993) and reaction progress variables (Chew et al., 1990). However, single laser sheet imaging techniques do have the inherent disadvantage that nothing is known of the flame in planes in front or behind the sheet. Movement of the flame kernel in the early stages of flame growth can result in a flame displacement well away from the laser sheet. With a single illuminating laser sheet it is often impossible to determine whether the sheet is slicing through the centre of the flame kernel. An understanding of these problems has existed since laser sheet measurements were first used within combustion systems and various solutions have been proposed to overcome the limitations of using single sheets. Yip et al. (1987) traversed a laser beam rapidly through an aerosol seeded gas jet with the use of a rotating mirror. However, since the images generated with such techniques are successive rather than simultaneous , in order to create a pseudo-instantaneous 3-D representation of the flame it is necessary that the laser sheet traverse speed is very high relative to the flow movement between images. Lawes et al. (1998) extended the method used by Yip et al. (1987) at faster laser repetition and data capture rates to map the turbulent flames in 3-D but did not analyze the imaged flames. In recent years, the number of consecutive imaged sheets has increased and this technique of sweeping a laser sheet across a volume of interest has been successfully applied to visualize fuel distribution in an engine (Nygren et al., 2002), soot volume fraction in non-premixed flames (Hult et al., 2002) and very recently to flames stabilized on a burner (Upton et al., 2011). Alternatively, more limited, instantaneous multiple sheet imaging has been achieved using, typically 4, sheets of different wavelengths generated simultaneously by Mantzaras et al. (1988).

Flames have been extensively modelled in 2 and 3-D by a number of workers who have characterized the flames using parameters such as $\sum$ and c. The Bray Moss Libby model (BML) (Bray et al., 1994) provides an expression for $\sum$ in terms of c, although there is no

reliable expression for the flame wrinkling scale required in the expression (Lee et al., 2000). The coherent flamelet model (CFM) (Maistret et al., 1989) has features to overcome some of the problems with BML although, according to Lee et al. (2000), it requires additional specific parameters for the turbulent diffusion; along with sink and source terms to close the transport equation. Other modelling approaches include use of the 'G equation' (Peters, 1999) and the stochastic particle/Monte Carlo concept (Pope and Cheng, 1986) as well as several others having similar features to those above. However, there is a scarcity of reliable fully resolved experimental data with which to compare the output of such modelling. Some experimental measurements of $\sum$, by direct and indirect means, have been published by (Lee et al., 2000; Bradley et al., 2009; Hult et al., 2007), but the indirect methods tend to require an additional relationship from one of the models to obtain $\sum$ (Lee et al., 2000), whilst direct measurements tend to be mostly 2-D. Often $\sum$ is determined by assuming that average surface area per unit volume equals the average flame perimeter per unit area in the laser sheet (Filatyev et al., 2005).

Historically, models have predicted the turbulent burning velocity with limited success, but now some convincing numerical experiments are being performed using Direct Numerical Simulations (DNS), which has given useful information on the structure of the turbulent flame brush (Driscoll, 2008). The advantage of DNS is that the three dimensional geometry and boundary conditions of a specific experiment are simulated with few modeling assumptions and high resolution, which can even resolve the Kolmogorov scale. In addition, DNS includes detailed chemistry and differential diffusion and employs no empirical constants. The applicability of DNS in the development of turbulent combustion models has been extensively reviewed by (Pointsot et al., 1995; Pointsot, 1996; Driscoll, 2008). When the DNS matched the experimental geometry and boundary conditions, good agreement between the turbulent burning velocity predicted by DNS and that measured for a V-flame was observed in Bell et al. (2005). Similarly, DNS of Bell et al. (2006) correctly predicted the

turbulent burning velocity measured in the Bunsen flame of Filatyev et al. (2005). However, a limitation with DNS is that realistic boundary conditions must be provided for all boundaries which often are unknown. For example, the assumption that the incoming turbulence is isotropic and has a corresponding power spectrum might not be always true, in which case it is necessary to measure all three integral scales, profiles of the fluctuations of all three velocity components and a measured power spectrum (Driscoll, 2008).

Clearly, turbulent combustion is complex and only partially understood. Since flame structures have been predominantly measured in 2-D, or modelled in 3-D, properties derived from these data may have associated inaccuracies. In the light of these limitations it is widely acknowledged, for example by (Driscoll, 2008; Hult et al., 2007), that there is a need for accurate 3-D images of turbulent flames; as well as calculation of the important structural parameters. The experiments reported here are designed to address the problems described above by using a multiple sheet mie-scattered light technique at very high laser repetition and data capture rates to successfully characterize a non-stabilized expanding turbulent flame kernel in 3-D. The raw data from the experiments are processed using a computer code to reconstruct the flame surface in 3-D thereby allowing parameters such as $\sum$ and c to be calculated. These values are subsequently compared to existing experimental and modelled data.

2. Experimental Techniques

2.1 Combustion Vessel

Combustion experiments were carried out in a spherical stainless steel vessel of 380 mm diameter; this was capable of withstanding the temperatures and pressures resulting from pre-explosion pressures and temperatures of 1.5 MPa and 600 K, respectively. The vessel had three pairs of orthogonally oriented windows made from fused quartz, with a 150 mm viewable aperture and thickness of 100 mm. These windows provided excellent optical access

for photographic and laser based measurements. Turbulence was generated in the vessel by 4 identical 8 bladed fans symmetrically disposed in a regular tetrahedron geometry. These fans were connected, via a shaft assembly, to 4, 8 kW electric motors. These had separate speed controllers, allowing accurate speed control to within ±2% of the set speed in order to generate spatially uniform turbulence intensity within the central region of the combustion vessel. The turbulent flow field was calibrated using laser doppler velocimetry (LDV) and particle image velocimetry (PIV) (Bradley et al., 1996). Measurements indicated that, within the optically accessed central region of 150 mm diameter, the turbulence was essentially isotropic with very low mean velocities. The rms turbulent velocity, u', was found to vary linearly with the fan speed. The turbulent integral length scale (L) was found directly from spatial correlation to be 20 mm and was independent of all operating variables (Bradley et al., 1996). The inner wall temperature of the vessel was measured by a 25 μ Chromel-Alumel wire, type K thermocouple, sheathed in a 1.5 mm diameter stainless steel tube. The accuracy of vessel wall temperature ranged from ±0.5 K at room temperature to ±2 K at higher temperatures, which resulted in a similar accuracy for mixture temperature determination. A Druck PDCR 911 static piezoresistive transducer was used to measure the pressure inside the vessel prior to combustion and to monitor the pre-ignition pressure of the combustible mixture. Equivalence ratio (ϕ) was determined by the method of partial pressures for methane-air mixtures.

2.2 Ignition System

Two ignition systems were used in the present work. Initially , an electronic system consisting of a Lucas 12 V transistorized car ignition coil system powered by a car battery was used. However, the spark electrode interfered with the image processing. Therefore laser ignition was adopted; this proved better, at the expense of increased experimental complexity. The laser ignition setup, detailed in (Bradley et al., 2004), was mounted on a large steel frame external to the vessel with the laser head sitting on a lower shelf and the beam being directed

upwards through a range of optics on the upper shelf and into the centre of the vessel. The laser was a Spectron Model SL800 pulsed Q-switched Nd:YAG utilizing a two stage arrangement with a separate oscillator and amplifier, which gave higher laser energies than single stage arrangements. In the present work, the laser was set up to give a 1064 nm (near infra red) beam of 600 mJ of 15 ns duration, with an average beam diameter of 6 mm. To ensure constant performance at the required energy, the laser was started at a repletion rate of 10 Hz for at least 60 seconds before triggering the experiment. This ensured thermal stability of the laser system.

2.3 Three Dimensional Laser Sheet Imaging

The technique works by creating multiple thin vertical laser sheets that pass through a flame inside the bomb, effectively creating 'slices' through the flame from left to right. The images generated by these slices were recorded on a digital camera and then reconstructed to create a 3-D model of the actual flame. Shown in Fig. 1 is a schematic of the optical arrangement. An Oxford Lasers copper vapor laser LS20-50, capable of repetition rates from 5 to 18 kHz, provided the pulsed light source. The pulse length was of the order of 20 ns and the pulse energy at 18 kHz, which was used throughout the present work, was typically 0.5 mJ. The beam from the laser passed through a 1000 mm focal length plano-convex lens to focus it to a point 10 mm in front of the rotating octagonal mirror to prevent damage to the mirror surface. Using a plano-convex cylindrical lens placed approximately 50 mm after the rotating mirror, a laser sheet of approximately 50 mm height was generated; this was translated across the central area within the combustion vessel using the rotating mirror. A 30 V AC and 6 A motor, capable of rotating the mirror at speeds between 300 and 15000 rpm, was used. The speed of rotation was measured using a helium neon laser pointed towards the octagonal mirror, a photo-diode was then positioned so that it detected the helium neon beam but not the copper vapor laser.

Images were recorded by a Photron Fastcam digital CCD camera, which was used at 18,000 fps with a chip size of 255*256 pixels. A Sony TV zoom lens, with an aperture of f 1.8 and focal length between 12.5 and 75 mm, was used. The large aperture resulted in a small depth of field which, unavoidably, caused parts of the image away from the focal point to be a little out of focus; however, this was preferable to the reduction in contrast between burned and unburned gas if a smaller aperture were to be used. A 510 nm interference filter was placed between the laser sheet and the camera lens to filter out background light from the combustion event; this was particularly intense as a result of emission of light from the seed as it heated. The resolution of approximately 0.7 mm in all three dimensions was considered reasonable in relation to the integral length scale (L) of 20 mm. It was adequate to resolve structures of the order of the Taylor scale (3 mm), although not those of the order of the Kolmogorov scale (0.15 mm). Synchronization of all the components (the laser for ignition, the copper vapor laser for imaging and the camera) was critical, as time resolved data of flames was required. This was achieved by using a laser diode and photo diode detector arrangement. The laser diode was reflected off the opposite face to that used by the copper vapor laser and was detected by the photo diode. This signal was sent to the camera, copper vapor laser and ignition source; such that they were all triggered at the same time.

2.4 Laser sheet geometry

Each face of the mirror generated one sweep through the combustion space with multiple laser firings (and images) per sweep. For a given laser repetition rate, the mirror speed determined both the sheet spacing and the number of sweeps through the combustion event. The lower the mirror speed the closer the sheets but the lower the number of sweeps that could be recorded of the flame. It was necessary to obtain a detailed understanding of the sheet geometry and its temporal variation, before analysis of 3-D images could be undertaken. A couple of issues need to be noted. Firstly, the rotating mirror produced a series of diverging sheets as shown in Fig. 1. As a result of sheet divergence, the laser sheet did not remain at a constant distance from the vessel centreline between the points where the sheet entered and

left the area of interest. An attempt was made to resolve this by placing a lens in between the mirror and the vessel window; however, that resulted in significant loss of intensity and hence was not implemented. Secondly, due to rotation of the mirror, the point of reflection varied in time. The geometrical offset produced due to both these issues was taken into account while analyzing the images with the implementation of a spatial transformation matrix in Matlab. Also, there was a finite time lag between the first flame image and the last flame image in one sweep of the laser sheet. Therefore it was important to select flames that were slow enough that they did not grow significantly during the time of sweep. For this reason, only mixtures having a low laminar burning velocity (u_l) and at low turbulence levels were investigated. In the present experiments, u'/u_l ranges between 1.11 to 6.22 while the ratio of integral length scale to the laminar flame thickness (L/δ_l) ranges between 111.75 to 447. Similarly, the Karlovitz number (K_λ, based upon the Taylor scale) ranges between 0.0235 to 0.371 while the Karlovitz number (K_η, based upon the Kolmogorov scale) varied between 0.47 and 7.42. Hence, the present data can be plotted in the corrugated flamelet and thin reaction zone regime on the modification of the Borghi diagram (Borghi, 1985) proposed by Peters (Peters, 2000). These conditions are considerably lower than those found in engines.

Lean turbulent methane-air flames were ignited in the centre of the vessel. The initial pressure and temperature were 0.1 MPa and 300 K respectively. Flames were imaged using mie-scattering (scattering of light off seed particles). The most successful seed was found to be olive oil, with a typical diameter of 1.06 μm and a density of 970 kg/m^3 (Melling, 1997). The olive oil seed particles were generated using a TSI 9306 six jet atomizer. This allowed particle concentrations of up to 10^(7) particles/cm with sizes between 0.01 and 2 μm. It was estimated that the number density of oil droplets in the mixture was 5*10^(-6) particles/cm^3 resulting in a mass concentration of 3.02*10^(-3) g. The same for methane was 1.17 g (at an

equivalence ratio, ϕ, of 0.6), hence the seed was not sufficient to significantly alter the burning rate of the mixture.

3. Image processing and data analysis

Laser sheet image processing required binarising and meshing of the multiple 2-D greyscale images to construct the 3-D flame structure; which further required surface smoothing before parameters such as c and $\sum$ could be evaluated.

3.1 Raw images

Shown in Fig. 2 is a typical set of raw mie scattering laser sheet images, separated by 0.7 mm in the third dimension, through a flame kernel at an "instant". Very little flame growth might be expected in the time interval of 1.4 ms covering the 25 images shown in Fig. 2. With a u_l of 0.09 m/s, the mean flame radius of this flame might be expected to grow by just 0.13 mm during this sweep. The spark plug is visible in the bottom left hand corner of the images and, in this combustion event, the kernel centroid can be seen to have migrated approximately "north north east". This migration is a function of the larger scales of turbulence at the spark gap at the instant of ignition and is random from one combustion event to another. Sheets 1 and 25 cut through the flame kernel close to its outer edges, Sheets 12-14 relate approximately to the centroid of the kernel with the spark gap centered on Sheet 13.

3.2 Binarising

The raw images shown in Fig. 2 had to be converted from their grayscale format, where each pixel could hold a value of between 0 (black) and 255 (white), to a series of binary images, where the pixels had values of either 0 (white) or 1 (black), to represent unburnt and burnt gas respectively. The binarising process was carried out in a number of stages. The last image prior to the first showing any flame was used as a background image to obtain the initial image brightness. This was then filtered, using an inbuilt function in Matlab, to remove noise

and smooth the image allowing for more consistent background brightness levels. The background image was then subtracted from the individual images in turn, leaving only the flame present. A threshold value was then applied to increase the image clarity and binarise the image resulting in a black flame surrounded by white.

3.3 Flame Surface Generation and Smoothing

In order to generate an image of the full 3-D flame, the binarised images were read into the Matlab environment, in numerical order, along with the image resolution and sheet separation. The Matlab software created an x, y, z matrix, with the x and y coordinates being the image size, and the z coordinate being the number of images, with the numerical value within each of these matrix cells being either 1 signifying burnt or 0 to signify unburnt. Once the matrix had been created, it was padded on all sides with two rows of pixels, value 0 (unburnt) to ensure a closed surface and volume. An inbuilt function within Matlab called 'isosurface' was used to create a surface within the volume of the flame between values that contained the same numerical value at each vertex, i.e. it connected together all the points on the boundary between the flame (value 1) and unburnt gas (value 0). Isosurfaces created were not smooth, as the thresholding and binarising procedures used to create the individual sheets often created flat areas and square edges. An algorithm of smoothing suggested by Taubin (Taubin, 1995), which maintained image quality and minimized shrinkage of shape whilst maximizing smoothing, was used to remove the surface imperfections. Shown in Fig. 3 are typical images of a reconstructed flame after surface smoothing, as seen from two different viewing angles. With a fully reconstructed 3-D flame, it was then possible to calculate values for a range of flame parameters.

3.4 Flame Parameters

In premixed combustion, a reaction progress variable (c) describes the progress of combustion in a premixed flame front and quantifies the extent of conversion from reactants to products, thereby allowing the transition between unburnt and burnt parts of the flame to be

visualized. The progress variable takes the value of zero in reactants and unity in products. Similarly, flame surface density ($\sum$) is defined as the flame surface area per unit volume. The turbulent burning velocity (u_t) for a flame is enhanced by an increase in the surface area of the reaction zone. The algorithm for the calculation of c and $\sum$ from the reconstructed 3-D flame is demonstrated through Fig. 4, where a cross section of the part of the 3-D flame surface is shown along with that of a spherical shell of inner and outer radii r_1 and r_2 respectively. The area of intersection of this shell radius with the 3-D flame at the radius r_2 is shown by dashed line. We denote this area as A_i. Similarly, the area of the annulus between r_1 and r_2, the cross section of which is represented by the dotted lines, is denoted as A_j. The value of c at a radius of r_2 is defined as:

$$c_{r_2} = \frac{\sum A_i}{4\pi {r_2}^2} \tag{1}$$

where $\sum A_i$ is the summation of A_i defined above. Similarly, the value of $\sum$ at a radius of $\frac{(r_1 + r_2)}{2}$ is defined as:

$$\sum_{\frac{(r_1+r_2)}{2}} = \frac{\sum A_j}{\frac{4\pi({r_2}^3 - {r_1}^3)}{3}} \tag{2}$$

where $\sum A_j$ is the summation of A_j defined above. The thickness of the spherical shell $(r_2 - r_1)$ was 2 mm and was optimized to minimize noise without excessively compromising resolution. The values of c and $\sum$ thus determined were recorded as a function of radii.

4. Results and Discussion

Analyzing the flame image data presented in Fig. 2, it is difficult to tell the shape of a flame from any given sheet, and even more difficult to determine its 3-D structure. Viewed using schlieren photography, such kernels appear almost spherical, however, the multiple sheet

images reveal considerable structure. This problem is further compounded by the appearance of two separate flames within one laser sheet, when in fact they may be joined together in another plane. An apparent island of flame can be observed in Frames 17, 18 and 19 in Fig. 2 giving an appearance of a fragmented or two separate flames. However, this can be seen to be interconnected with the main kernel in Frame 16. Hicks et al. (1994), noticed that smaller scales could give the appearance of islands in front of the main reaction event that have apparently been ripped away from the main flame. Likewise small pockets can appear behind the reaction front. For example, a pocket of mixture appears inside the flame in Frames 9 and 10 in Fig. 2, but again this is seen connected with the outside unburned gas in Frame 8. Unless very high turbulent levels have been achieved, these apparent islands and pockets are in fact fingers of unburned/burned mixture interconnected to other gas regions on different planes within the vessel (Hicks et al., 1994; Mantzaras et al., 1988; Gillespie et al., 2000).

4.1 Reaction Progress

Shown in Fig. 5 is the variation of c with radius from the instantaneous flame centroid for 7 methane–air flames at ϕ=0.8, u'=0.4 m/s and 8 ms after ignition. These data include all acceptable measurements obtained during the present work at this condition. Each curve exhibits the expected profile, in that it progresses asymptotically to a value of unity (representing fully burned gas) at smaller radii and towards zero at larger radii in the unburned gas. The root radius of the flame is given by the largest radius at which c=1 and the tip radius is given by the maximum radius at which c>0. A useful representative flame radius, used by Bradley et al. (2003) is that at which c=0.5 and denoted by $r_{c=0.5}$. This represents the radius at which the volume of burned gas outside that radius is equal to the volume of unburned gas inside (Bradley et al., 2003). For the data in Fig. 5, the average value of $r_{c=0.5}$ is 11 mm, while the horizontal bar showing the variability of $r_{c=0.5}$ measures 4 mm. All these flames lie approximately within the radii ranging between 4 to 20 mm. Even at identical experimental conditions and near isotropic turbulence, the flames were quite

different in shape with a variation of almost 23% in the average flame diameter. This gives an approximate measure of experimental variability in the very well controlled environment of the fan stirred bomb and at levels of turbulence that are quite low when compared with an engine running at moderate speed.

It seems logical to assume that the turbulent flame brush thickness (δ_t), and hence the profile of c, will be a function of turbulence length scale (L). Therefore, although L does not vary in the present work, c is plotted against the dimensionless form of r/L in Figs. 6(a) and (b). While Fig. 6(a) presents results at various times after ignition for methane-air flames at ϕ=0.7 (u_l=0.17 m/s) and u'=0.4 m/s, Fig. 6(b) does the same for ϕ=1.0 (u_l=0.36 m/s) and u'=0.4 m/s. Hence, Figs. 6(a) and (b) represent curves at high and low values of u'/u_l respectively. The trends are similar to those in Fig. 5. Although the root radius varies little with a value between 0.15 and 0.4 regardless of time after ignition, the tip radius changes dramatically with time after ignition. It is interesting to note that the asymptotic progression to c=1 for the larger flames in Figs. 6(a) is less well defined than for the smaller flame. At 8 ms after ignition in Fig. 6(a), the tip radius is at approximately 0.5, giving a difference in extremities of the flame as approximately 0.4. This difference in extremities of the flame gradually increases from 0.4 to 1.5 at 25 ms after ignition, being 1 at 16 ms after ignition. At 33 ms seconds after ignition, the tip radius is at approximately 2.2, giving the difference between extremities of the flame as approximately 2. This indicates that as time from ignition increases and the flame develops, δ_t increases. That the flame increases in thickness during this developing period is not unexpected, as the effect of turbulence is more evident because an increase in the flame size leaves more surface area for the turbulence to act on, leading to an increase in wrinkling. However, the very small change in root radius is surprising. The variability of $(r/L)_{c=0.5}$ is greater for the larger flame represented in Fig. 6(a) which might be expected. Figure 6(b) shows similar trends, again the root radius seems to remain

approximately constant whilst the tip radius increases with time from ignition. The variation of c with r/L for the curve in Fig. 6(a) after 33 ms is similar in magnitude to that of the curve in Fig. 6(b) after 12 ms. This shows that the flames in Fig. 6(a) are considerably slower than those in Fig. 6(b). The data from Figs. 6(a) and (b) can be used to calculate the turbulent flame speed (S_t). This is shown in Fig. 7, where the flame radius at c =0.5, denoted by $r_{c=0.5}$, is plotted against time after ignition for ϕ =0.7, 0.8 and 1.0 of methane-air mixtures. The data points at each of the given ϕ are reasonably fitted with a linear curve as shown in Fig. 7. The value of S_t is then calculated as the slope of the linear fit, which was measured to be 0.79, 0.94 and 2.32 m/s for ϕ =0.7, 0.8 and 1.0 respectively.

The present results do not confirm the validity of the normalized parameters in Figs. 6(a) and (b) because the present vessel had a constant L. The ratio of $r/r_{c=0.5}$, in which r is the flame radius and $r_{c=0.5}$ is the radius at c =0.5, proved to be a better normalization parameter; which is demonstrated in a good generalization in Fig.8(a), which shows the data from Fig. 6(a) plotted against $r/r_{c=0.5}$. An interesting observation from Fig. 8(a) is that the gradient of c against $r/r_{c=0.5}$ appears to be a maximum near to c =0.5. A similar generality is observed for ϕ equal to 0.8 and 1.0 as well. An average curve of the four individual curves in Fig. 8(a) was generated. Similarly, such an average curve was also generated at ϕ =0.8 and 1.0. These three average curves at ϕ =0.7, 0.8 and 1.0 corresponding to u'/u_l =2.35, 1.67 and 1.11 respectively, are shown in Fig. 8(b). Figure 8(b) illustrates how δ_t, indicated by the profile of c, increases for progressively leaner mixtures at values of c <0.5. Additionally, leaner flames tend to become more asymmetric with the gradient being lower at the unburnt side of c =0.5 than at the burnt side. Coincident with this is a trend for the maximum gradient, which equates to the location of maximum burning rate, shifting towards the burned gas. It is

probable that the increase in thickness at c <0.5 is probably due to the interaction between laminar-like burning and turbulence, rather than due to ϕ alone.

4.2 Flame Surface Density

Following Hult et al. (2007), generality is achieved by plotting $\sum$ multiplied by the laminar flame thickness (δ_l). As with Figs. 6(a) and (b), r is normalized by L. Figure 9(a) presents the variation of average value of normalized flame surface density ($\Sigma\delta_l$), with normalized radius (r/L), corresponding to the data presented in Fig. 6(a). The overall shape of the curves is, to a first approximation, of a Gaussian form. Each curve in Fig. 9(a) exhibits a similar and expected profile in which $\Sigma\delta_l$ is zero in fully burned gas. It then increases to a maximum value before returning back to zero in the unburned gas. The root radius remains approximately constant but the distribution of $\Sigma\delta_l$ increases with time, manifested in the increasing profile width. However, as the effective turbulence seen by the flame increases with time, the maximum value of $\Sigma\delta_l$ decreases with increasing time from ignition; with the maximum value reducing from 0.52 at 8 ms after ignition to 0.23 at 33 ms. This is consistent with an assumption that a thin laminar flame would have a very narrow, but high magnitude distribution of $\Sigma\delta_l$ with flame radius, whereas a turbulent flame has a greater thickness and hence a lower $\Sigma\delta_l$. Similar trends are shown in Fig. 9(b) which corresponds to the data presented in Fig. 6(b). As with Figs. 8(a) and (b), an alternative parameter for normalization could be $r_{c=0.5}$. The justification for this is that δ_t, and hence distribution of $\Sigma\delta_l$, increases as the flame develops; and this is more directly a function of flame size than of the turbulence. Shown in Fig. 10(a) are values of $\Sigma\delta_l$ plotted against $r_{c=0.5}$ for the data presented in Fig. 9(a). This figure shows a better generalization, particularly for those flames at 16, 25, and 33 ms after ignition; suggesting that for the conditions in the present work, the normalized reaction zone profile varies little with flame radius. A similar generality is also observed in

Fig. 10(b), in which the normalization with $r_{c=0.5}$ is implemented for the data presented in Fig. 9(b).

The variation of normalized flame surface density ($\Sigma\delta_l$) across the flame brush is shown in Fig. 11(a) and (b) for methane-air mixtures at ϕ=0.7 and 1.0 respectively, at different time after ignition. In both the figures, the maximum value of $\Sigma\delta_l$ decreases consistently at increasing time from ignition because the effective turbulence seen by the flame increases with time and, hence the flame gets more dispersed. However, at later times (for time>16 ms for ϕ=0.7 and time>6 ms for ϕ=1.0) the shapes of $\Sigma\delta_l$ curves tend to become independent of time. At these later times, the mean flame diameter (2* $r_{c=0.5}$) is larger than L. Hence, the flame encompasses all scales of the turbulent flow and does not see any new turbulence as it grows. Additionally, values of $\Sigma\delta_l$ in Fig. 11(b) are lower than those in Fig 11(a) by almost a factor of 2. This is because the surface area density results from a competition between flame propagation (u_l) and flame wrinkling due to turbulence (u'). Therefore, it is not surprising that the maximum of $\Sigma\delta_l$ goes down by a factor of 2 when the ratio u'/u_l also goes down by a factor of 2 (i.e. from 2.35 to 1.11). Furthermore, Lawn and Schefer (2006) pointed out that nearly all studies relating to the structure of turbulent flames have found that $\sum$ varies across the flame brush as:

$$\Sigma = 4\Sigma_{\max} c(1-c) \qquad (3)$$

where $\Sigma_{\max}$ is the $\sum$ at the centre of the brush where c=0.5. A curve which utilized Eq. (3) for the time of 9 ms is shown by the thick solid line in Fig. 11(b). There is a very good agreement between Eq. (3) and the experimental data.

4.3 Comparison with other works

Driscoll (2008) suggested that real flames undergo "geometry-dependent" wrinkling implying that only flames within a particular geometrical category should be compared. For example, the wrinkling process and boundary conditions for spherical flames might be inherently different to those for envelope and flat flames on a Bunsen and counterflow burner respectively. Except for the present work, the present authors are unaware of any transient 3-D measurements of a turbulent flame developing from a point source of ignition in isotropic turbulence. However, Hult et al. (2007) did 2-D FSD measurements in premixed turbulent methane-air flame kernels in a similar geometry and also modelled such conditions with 3-D DNS using single step chemistry. The turbulence levels investigated in Hult et al. (2007) permit a comparison with the present measurements. Figure 12 presents the results of PLIF and the DNS from Hult et al. (2007) along with the present measurements at approximately similar u'/u_l , close to 1.7. The curves corresponding to the PLIF and present experiments represent the average variation of $\Sigma\delta_l$ with c . The DNS data corresponds to 2 eddy turn over times after initialization. It can be seen from Fig. 12 that there is excellent agreement between the PLIF data and the present measurements. Furthermore, the DNS data profile is qualitatively similar to that of the experiments. However, the maximum value of $\Sigma\delta_l$ in the experimental data is six times smaller than that obtained from the DNS. Hult et al. (2007) attribute this deviation to the difference in the length scale ratio (L/δ_l) between their PLIF experiments and the DNS. The length scale ratio for the present experiments was close to 447 in comparison to 1.7 for the DNS. Further work is required to substantiate this proposition.

5. Summary

Measurements of spherically expanding flame fronts in constant volume combustion vessels are complicated by flame development. Movement of the flame in the early stages of growth can lead to the flame moving away from the laser sheet. Although 2-D experiments are often designed to image the centre slice through a flame, flame movement is 3-D, and it is difficult

to know exactly what part of the flame has been captured. In the present work, flames have been mapped in 4-D (3-D in space and 1-D in time) to resolve the inadequacies inherent in 2-D techniques. Full construction of a turbulent flame from a series of laser sheets allowed accurate measurements of values for flame surface area, reaction progress variable and turbulent flame brush thickness. Experiment to experiment variation in flame development was demonstrated by both sheet images and their 3-D reconstructions. The reasonable qualitative agreement with published experimental and DNS data encourage similar investigation at higher turbulence levels. The technique could be further developed to incorporate more laser sheets per flame, possibly with either a different laser, or two laser and camera systems which will ultimately increase the resolution of the images by reducing the sheet separation distance. This will allow for faster burning mixtures or higher turbulence levels, which are of direct relevance to engines, to be imaged more accurately.

Acknowledgments

Some of this work was undertaken as part of an EPSRC, Jaguar and Shell funded project "Combustion Concepts for Sustainable Premium Vehicles". The authors would like to acknowledge this financial support. The authors are also grateful to Mr. Brian Leach for technical assistance.

References

[1] Abdel-Gayed, R.G., Bradley, D., and Lawes, M. (1987) Turbulent burning velocities: a general correlation in terms of straining rates. *Proc. R. Soc. Lond*., A 414, 389.

[2] Aleiferis, P.G., Taylor, A.K.M.P., Ishii, K., and Urata, Y. (2004) The nature of early flame development in a lean-burn stratified-charge spark-ignition engine. *Combust. Flame*, **136**, 283.

[3] Vermorel, O., Richard, S., Colin, O., Angelberger, C, Benkenida, A, and Veynante, D. (2009) Towards the understanding of cyclic variability in a spark ignited engine using multi-cycle LES. *Combust. Flame*, **156**, 1525.

[4] Lefebvre, A.H. (1999) Gas Turbine Combustion, 2nd Edition, Taylor and Francis, London.

[5] Bradley, D., Lawes, M., and Mansour, M.S. (2011) Correlation of turbulent burning velocities of ethanol-air, measured in a fan-stirred bomb up to 1.2 MPa. *Combust. Flame*, **158**, 123.

[6] Lipatnikov, A.N., and Chomiak, J. (2002) Turbulent flame speed and thickness: phenomenology, evaluation, and application in multi-dimensional simulations. *Prog. Energy Combust. Sci*., **28**, 1.

[7] Halter, F., Chauveau, C., Gokalp, I., and Veynante, D. (2009) Analysis of flame surface density measurements in turbulent premixed combustion. *Combust. Flame*, **156**, 657.

[8] Bray, K., Domingo, P., and Vervisch, L. (2005) Role of progress variable in models for partially premixed turbulent combustion. *Combust. Flame*, **141**, 431

[9] Chakraborty, N., Hawkes, E.R., Chen, J.H., and Cant, R.S. (2008) The effects of strain rate and curvature on surface density function transport in turbulent premixed methane-air and hydrogen-air flames: A comparative study. *Combust. Flame*, **154**, 259.

[10] Hicks, R.A., Lawes, M., Sheppard, C.G.W., and Whitaker, B.J. (1994) Multiple laser sheet imaging investigation of turbulent flame structure in a spark ignition engine. *SAE paper* 941992.

[11] Lee, T.W., North, G.L., and Santavicca, D.A. (1993) Surface properties of turbulent premixed propane/air flames at various Lewis numbers. *Combust. Flame*, **93**, 445.

[12] Chew, T.C., Bray, K.N.C., and Britter, R.E. (1990) Spatially resolved flamelet statistics for reaction rate modeling. *Combust. Flame*, **80**, 65.

[13] Yip, B., Lam, J.K., Winter, M., and Long, M.B. (1987) Time-resolved three-dimensional concentration measurements in a gas jet. *Science*, **235**, 1209.

[14] Lawes, M., Sheppard, C.G.W., and Woolley, R. (1998) Three-dimensional mapping of turbulent flame fronts. Ninth International Symposium on Applications of Laser Techniques to Fluid Mechanics, Lisbon, July 13-16, **2**, 35.2.1.

[15] Nygren, J., Hult, J., Richter, M., Aldén, M., Christensen, M., Hultqvist, A., and Johansson, B. (2002) Three-dimensional laser induced fluorescence of fuel distributions in an HCCI engine. *Proc. Combust. Instit*., **29**, 679.

[16] Hult, J., Omrane, A., Nygren, J., Kaminski, C.F., Axelsson, B., Collin, R., Bengtsson, P.-E., and Aldén, M. (2002) Quantitative three-dimensional imaging of soot volume fraction in turbulent non-premixed flames. *Experiments in Fluids*, **33**, 265.

[17] Upton, T.D., Verhoeven, D.D., and Hudgins, D.E. (2011) High-resolution computed tomography of a turbulent reacting flow. *Experiments in Fluids*, **50**, 125.

[18] Mantzaras, J., Felton, P.G., and Bracco, F.V. (1988) Three-Dimensional Visualization of Premixed-Charge Engine Flames: Islands of Reactants and Products; Fractal Dimensions; and Homogeneity. *SAE paper* **881635**.

[19] Bray, K.N.C., and Peters, N. (1994) Laminar Flamelets in turbulent flames. In Libby, P.A., and Williams, F.A. (Ed.) *Turbulent Reacting Flows*, Academic Press, London, pp. 63–114.

[20] Lee, G.G., Kang, Y.H., and Kobayashi, H. (2000) Measurement and analysis of flame surface density for turbulent premixed combustion on a nozzle-type burner. *Combust. Flame*, **122**, 43.

[21] Maistret, E., Darabiha, N., Poinsot, T., Veynante, D., Lacas, F., Candel, S., and Esposito, E. (1989) Recent developments in the coherent flamelet description of turbulent combustion. In Dervieux, A., and Larrouturou, B. (Ed.) *Numerical Combustion*, Springer-Verlag, Berlin, pp. 98–117.

[22] Driscoll, J.F. (2008) Turbulent premixed combustion: Flamelet structure and its effect on turbulent burning velocities. *Prog. Energy Combust. Sci*., **34**, 91.

[23] Peters, N. (1999) The turbulent burning velocity for large-scale and small-scale turbulence. *Journal of Fluid Mechanics*, **384**, 107.

[24] Pope, S.B., and Cheng, W.K. (1986) Statistical calculations of spherical turbulent flames. *Proc. Combust. Instit*., **21**, 1473.

[25] Bradley, D., Lawes, M. and Mansour, M.S. (2009) Flame surface densities during spherical turbulent flame explosions. *Proc. Combust. Instit*., **32**, 1587.

[26] Hult, J., Gashi, S., Chakraborty, N., Klein, M., Jenkins, K.W., Cant, S., and Kaminski, C.F. (2007) Measurement of flame surface density for turbulent premixed flames using PLIF and DNS. *Proc. Combust. Instit*., **31**, 1319.

[27] Filatyev, S.A., Driscoll, J.F., Carter, C.D., and Donbar, J.M. (2005) Measured properties of turbulent premixed flames for model assessment, including burning velocities, stretch rates and surface densities. *Combust. Flame*, **141**, 1.

[28] Poinsot T, Candel S, Trouve A. (1995) Applications of direct numerical simulations to premixed turbulent combustion. *Prog Energy Combust Sci*., **21**, 531.

[29] Poinsot T. (1996) Using direct numerical simulations to understand premixed turbulent combustion. *Proc. Combust. Instit*., **26**, 219.

[30] Bell J.B., Day M.S., Shepherd I.G., Johnson M.R., Cheng R.K., Grcar J.F., Beckner V.E., and Lijewski M.J. (2005) Numerical simulation of a laboratory scale turbulent V-flame. *Proc. Natl. Acad. Sci*., **102**, 10006.

[31] Bell JB, Day MS, Grcar JF, Lijewski MJ, Driscoll JF, Filatyev SA. (2006) Numerical simulation of a laboratory-scale turbulent slot flame. *Proc. Combust. Instit*., **31**, 1299.

[32] Bradley, D., Lawes, M., Sheppard, C.G.W., and Woolley, R. (1996) Study of turbulence and combustion interaction: Measurement and prediction of the rate of turbulent burning. Technical Report, University of Leeds, Leeds, UK.

[33] Bradley, D., Sheppard, C.G.W., Suardjaja, R., and Woolley, R. (2004) Fundamentals of high-energy spark ignition with lasers. *Combust. Flame*, **138**, 55.

[34] Borghi, R. (1985) On The Structure And Morphology Of Turbulent Premixed Flames. *Recent Adv. in the Aerosp. Sci*., 117-138.

[35] Peters, N. (2000) Turbulent Combustion. Cambridge University Press.

[36] Melling, A. (1997) Tracer particles and seeding for particle image velocimetry. *Measurement Science and Technology*, **8**, 1406.

[37] Taubin, G. (1995) A signal processing approach to fair surface design. Proceedings of the Fifth International Conference on Computer Vision, Washington DC, USA. IEEE Computer Society. ISBN 0-8186-7042-8.

[38] Gillespie, L., Lawes, M., Sheppard, C.G.W., and Woolley, R. (2000) Aspects of Laminar and Turbulent Burning Velocity Relevant to SI Engines. *SAE paper* **2000-01-0192**.

[39] Bradley, D., Haq, M.Z., Hicks, R.A., Kitagawa, T., Lawes, M., Sheppard, C.G.W., and Woolley, R. (2003) Turbulent burning velocity, burned gas distribution, and associated flame surface definition. *Combust. Flame*, **133**, 415.

[40] Lawn, C.J., and Schefer, R.W. (2006) Scaling of premixed turbulent flames in the corrugated regime. *Combust. Flame*, **146**, 180.

Figure Captions

Figure 1. Schematic of multiple laser sheet (swinging sheet) imaging set up.

Figure 2. Twenty five "slices" through the flame at one instant. Methane-air mixture at ϕ=0.6, u'/u_l =6.22 and 28.9 ms from ignition. The dimension of each frame is 128*64 pixels which is equivalent to 90*45 mm. The frames are separated by 0.7 mm in the third dimension.

Figure 3. Typical image of a reconstructed flame after surface smoothing viewed from two different angles.

Figure 4. A cross section of the part of the 3-D flame surface showing the burned and unburned region along with a spherical shell of inner and outer radii r_1 and r_2 respectively.

Figure 5. Variation of RPV against radius from instantaneous flame centroid at 8 ms after ignition for methane-air mixture at ϕ=0.8 and u'/u_l =1.67. Data presented from seven explosions at nominally identical experimental conditions. Turbulent flame thickness (δ_t) measured between c=0.1 and 0.9.

Figure 6. RPV plotted against normalized radius (r/L) at different time after ignition for methane-air mixture. Figure (a) at ϕ=0.7, u'/u_l =2.35 and (b) at ϕ=1.0, u'/u_l =1.11. Arrows showing the extent of experimental variation at c=0.5.

Figure 7 Flame radius at c=0.5, denoted by $r_{c=0.5}$, plotted against time after ignition for ϕ=0.7, 0.8 and 1.0 of methane-air mixtures. Turbulent flame speed (S_t) calculated as the slope of the linear fit through the data points at a given ϕ.

Figure 8. (a) showing RPV plotted against normalized radius ($r/r_{c=0.5}$) at different time after ignition for methane-air mixture at ϕ=0.7, u'/u_l =2.35. Figure (b) shows the average of the curves presented in (a) along with the average curve generated at other u'/u_l .

Figure 9. Normalized FSD ($\Sigma\delta_l$) plotted against normalized radius (r/L) at different time after ignition for methane-air mixture. Figure (a) at ϕ=0.7, u'/u_l =2.35 and (b) at ϕ=1.0, u'/u_l =1.11.

Figure 10. Normalized FSD ($\Sigma\delta_l$) plotted against normalized radius ($r/r_{c=0.5}$) at different time after ignition for methane-air mixture. Figure (a) at ϕ=0.7, u'/u_l =2.35 and (b) at ϕ=1.0, u'/u_l =1.11.

Figure 11. Normalized FSD ($\Sigma\delta_l$) plotted against RPV at different time after ignition for methane-air mixture. Figure (a) at ϕ=0.7, u'/u_l =2.35 and (b) at ϕ=1.0, u'/u_l =1.11. $\Sigma\delta_l$ calculated using Eq. (3) at 9 ms is shown as a thick solid line in Fig. (b).

Figure 12. Variation of normalized FSD ($\Sigma\delta_l$) with RPV. Present measurements shown in solid line for methane-air mixture at ϕ=0.8, u'/u_l =1.67. Comparison with 2-D PLIF and 3-D DNS shown in short-dotted and dash-dotted line respectively at comparable u'/u_l . The DNS and PLIF data for methane-air mixture are taken from Hult et al. (2007).

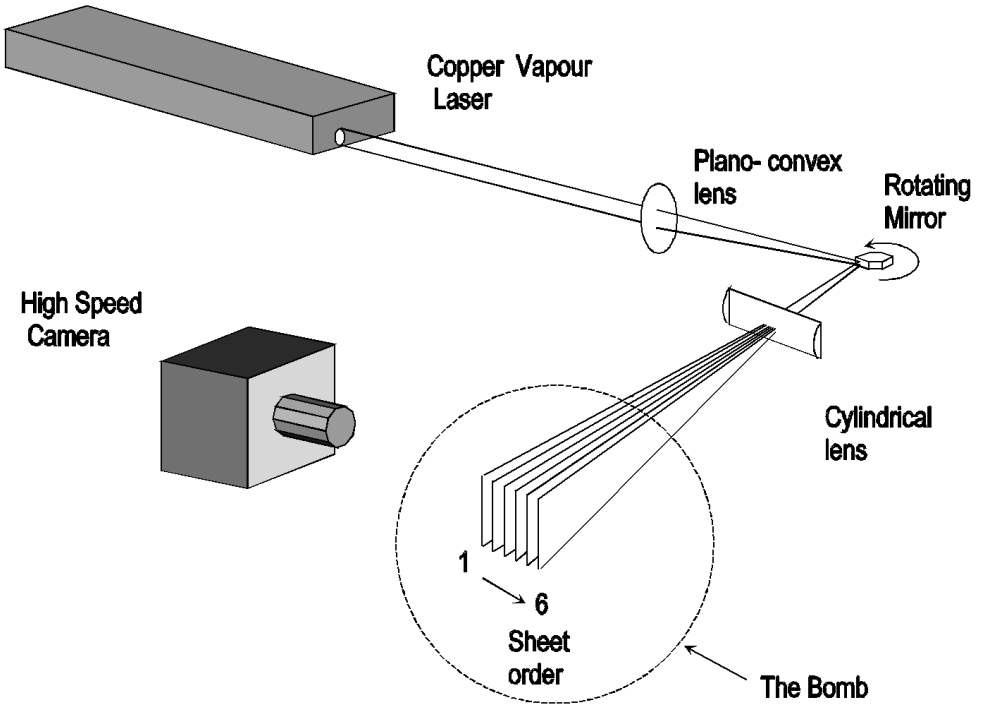

Figure 1. Schematic of multiple laser sheet (swinging sheet) imaging set up.

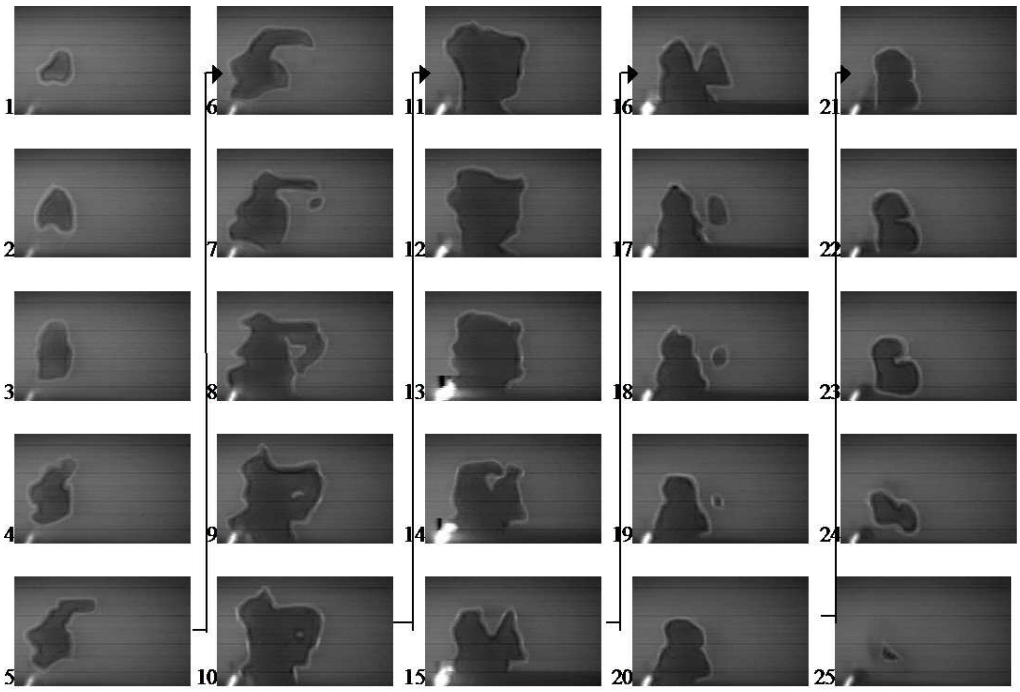

Figure 2. Twenty five "slices" through the flame at one instant. Methane-air mixture at ϕ=0.6, u'/u_l =6.22 and 28.9 ms from ignition. The dimension of each frame is 128*64 pixels which is equivalent to 90*45 mm. The frames are separated by 0.7 mm in the third dimension.

Figure 3. Typical image of a reconstructed flame after surface smoothing viewed from two different angles.

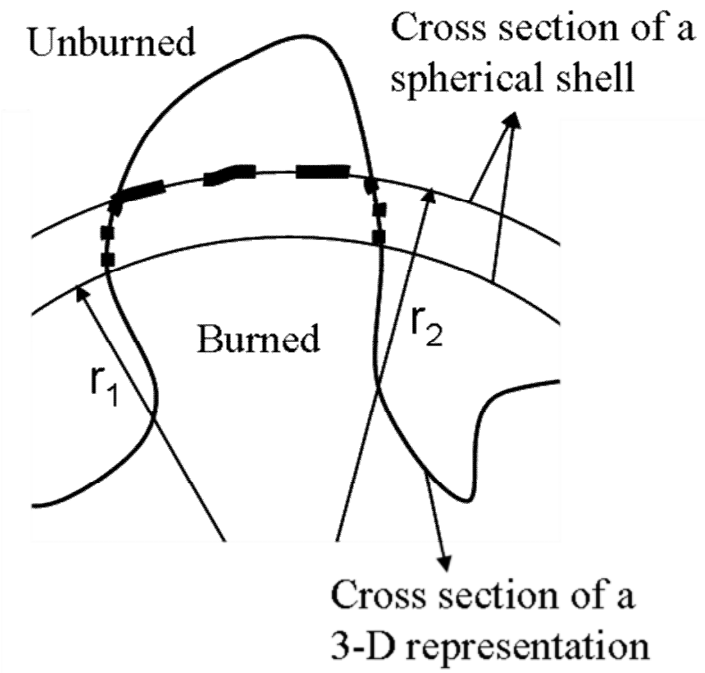

Figure 4. A cross section of the part of the 3-D flame surface showing the burned and unburned region along with a spherical shell of inner and outer radii r_1 and r_2 respectively.

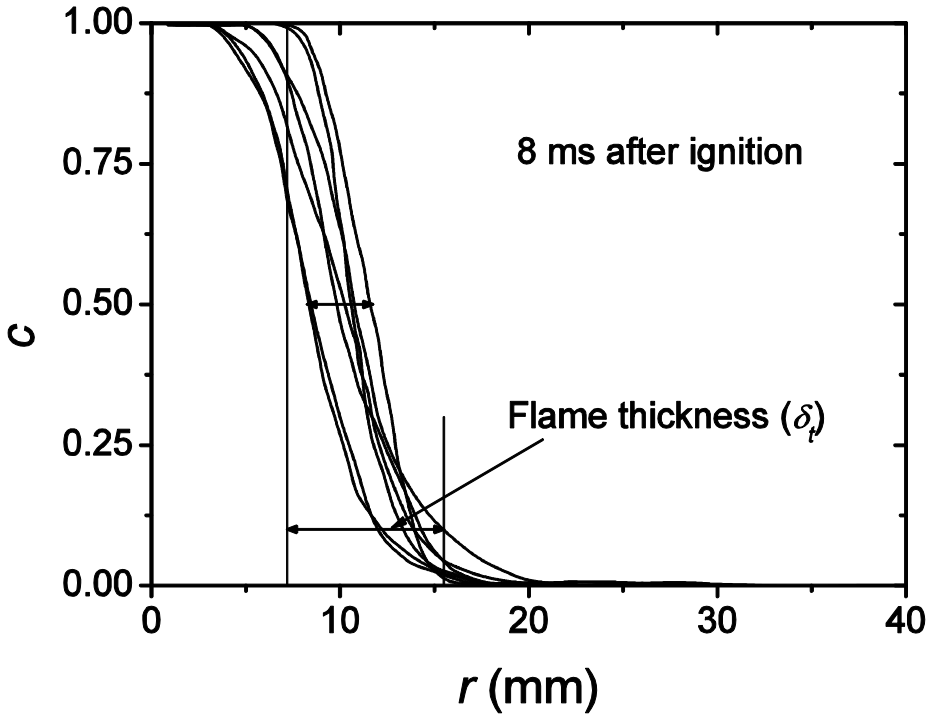

Figure 5. Variation of RPV against radius from instantaneous flame centroid at 8 ms after ignition for methane-air mixture at ϕ=0.8 and u'/u_l =1.67. Data presented from seven explosions at nominally identical experimental conditions. Turbulent flame thickness (δ_t) measured between c =0.1 and 0.9.

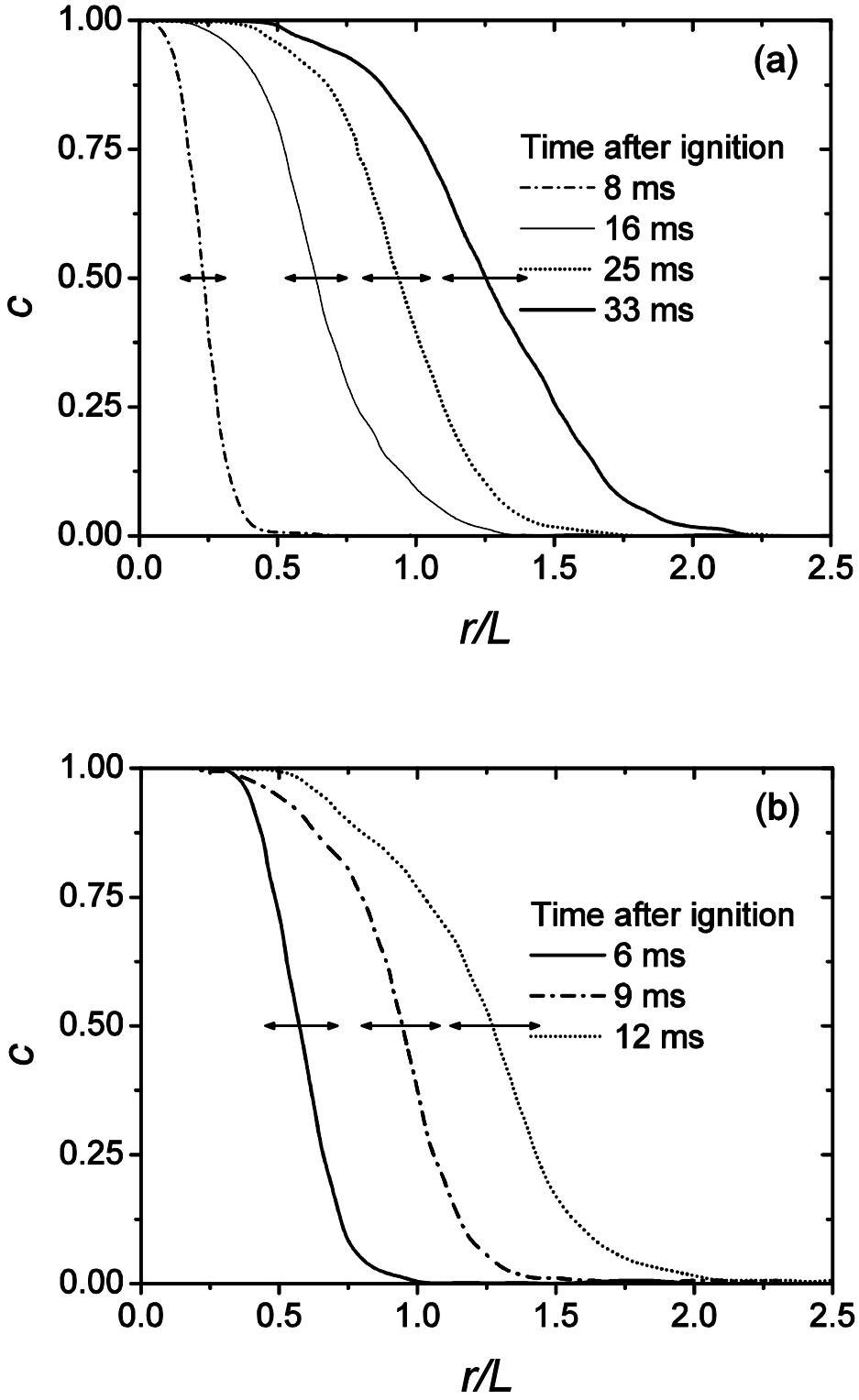

Figure 6. RPV plotted against normalized radius (r/L) at different time after ignition for methane-air mixture. Figure (a) at ϕ=0.7, u'/u_l =2.35 and (b) at ϕ=1.0, u'/u_l =1.11. Arrows showing the extent of experimental variation at c=0.5.

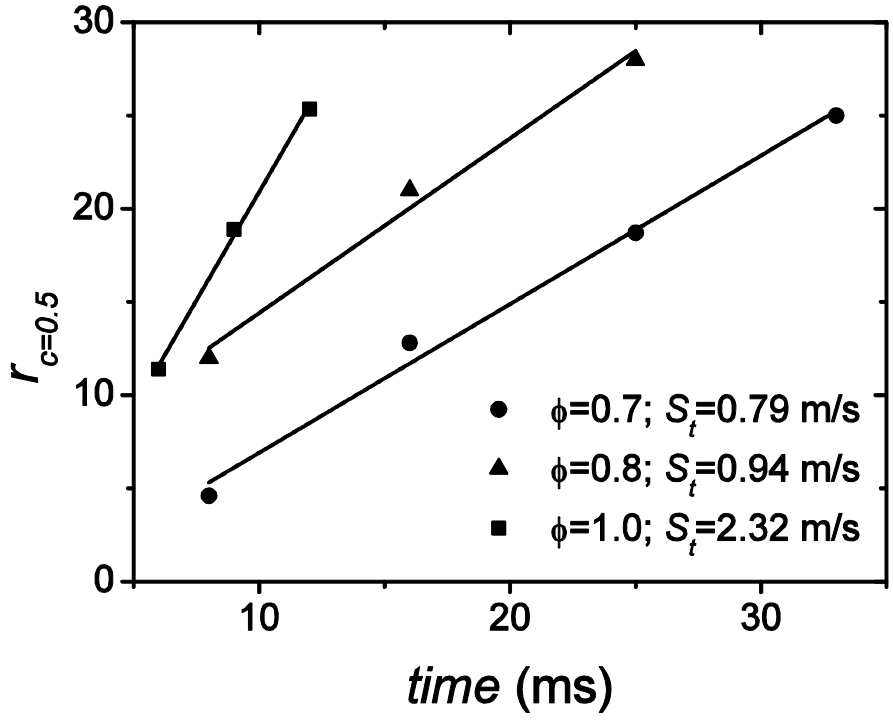

Figure 7 Flame radius at c=0.5, denoted by $r_{c=0.5}$, plotted against time after ignition for ϕ=0.7, 0.8 and 1.0 of methane-air mixtures. Turbulent flame speed (S_t) calculated as the slope of the linear fit through the data points at a given ϕ.

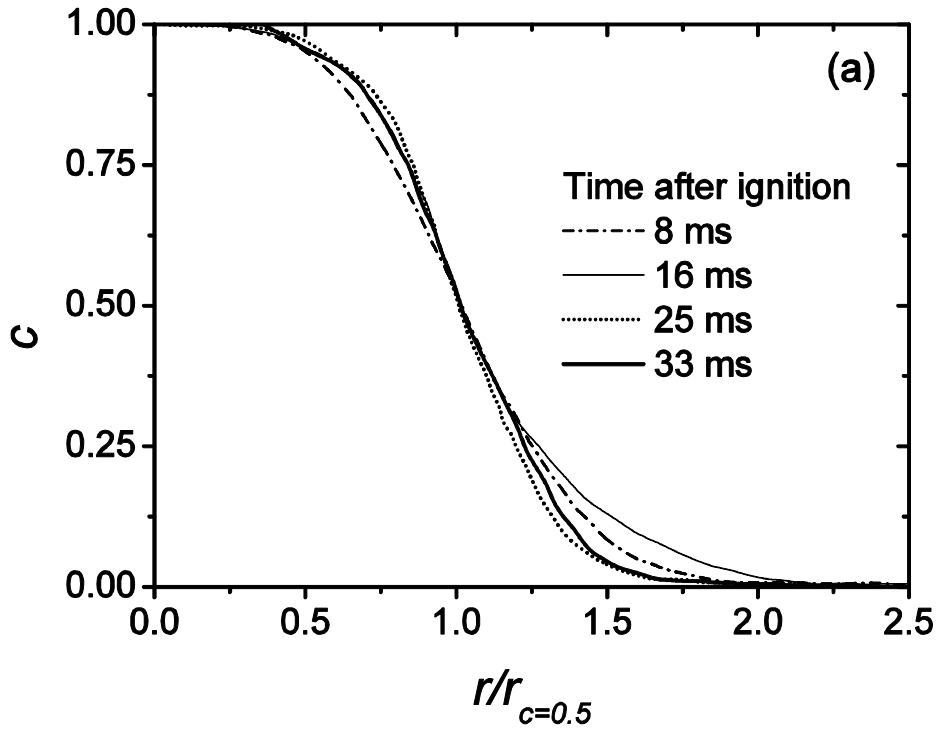

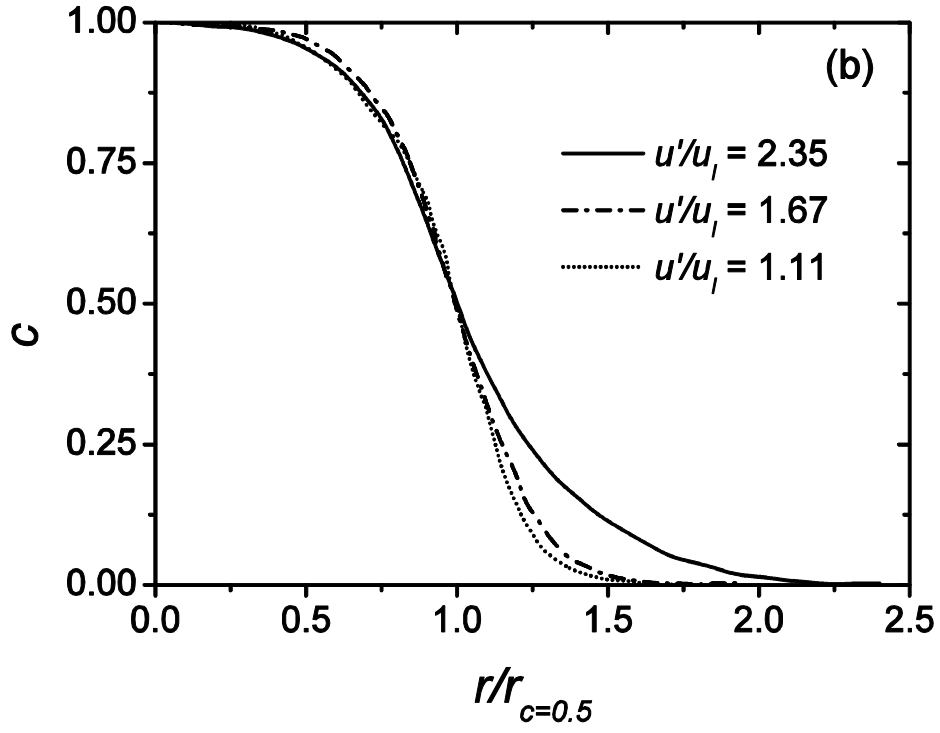

Figure 8. (a) showing RPV plotted against normalized radius ($r/r_{c=0.5}$) at different time after ignition for methane-air mixtures at ϕ =0.7, u'/u_l =2.35. Figure (b) shows the average of the curves presented in (a) along with the average curve generated at other u'/u_l .

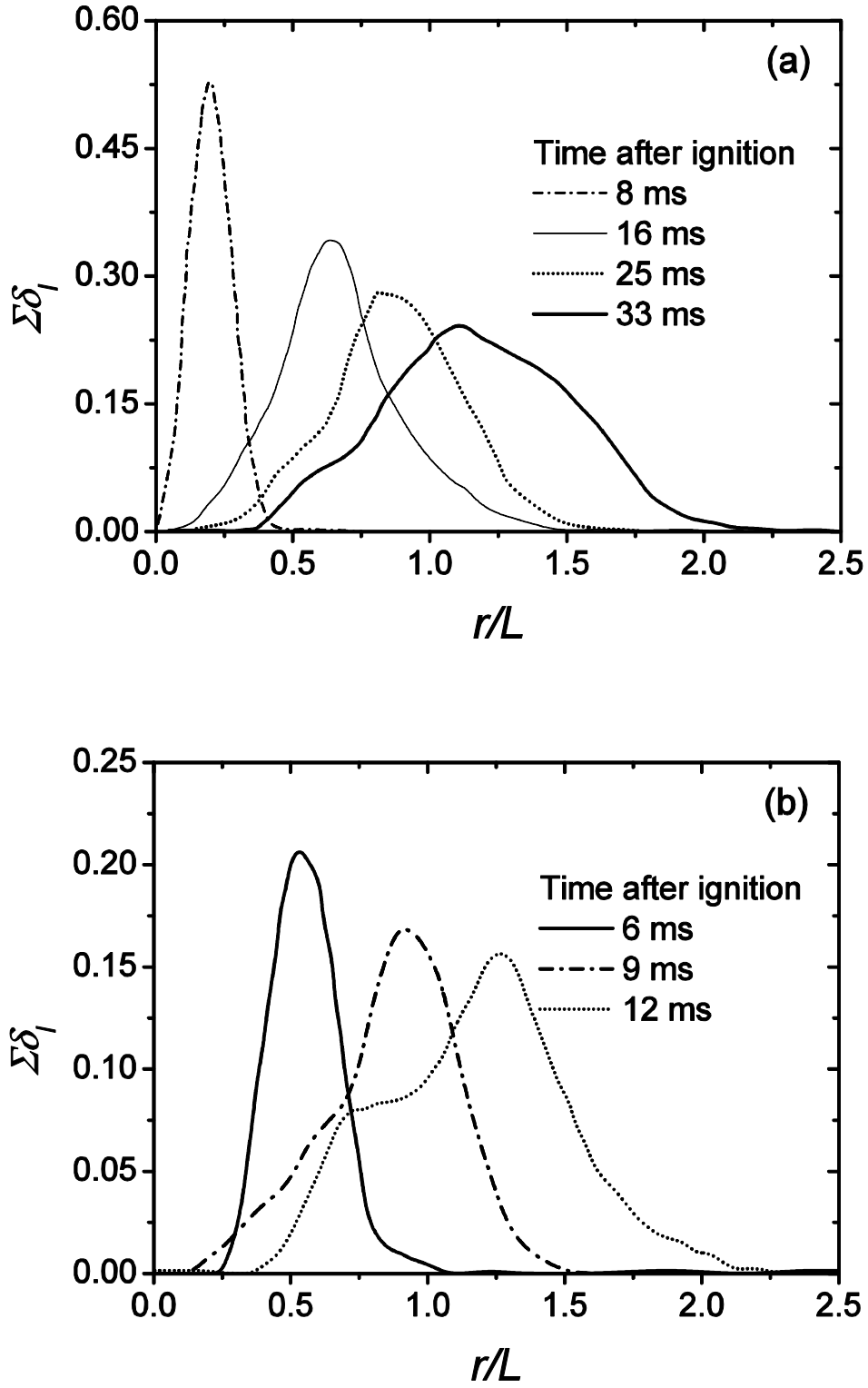

Figure 9. Normalized FSD ($\Sigma\delta_l$) plotted against normalized radius (r/L) at different time after ignition for methane-air mixture. Figure (a) at ϕ=0.7, u'/u_l =2.35 and (b) at ϕ=1.0, u'/u_l =1.11.

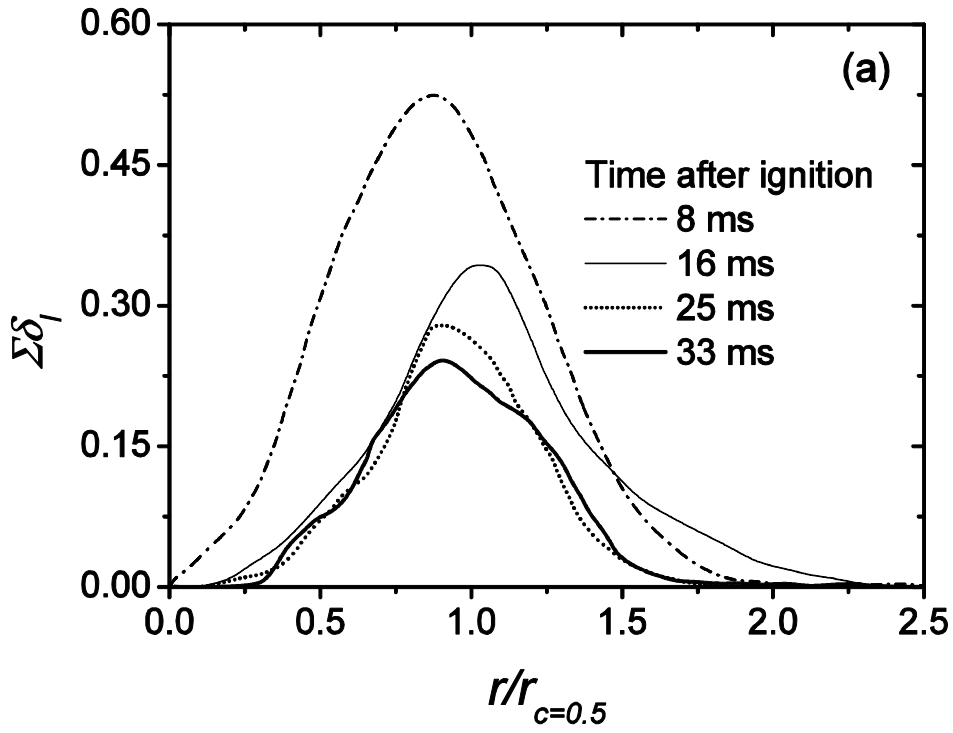

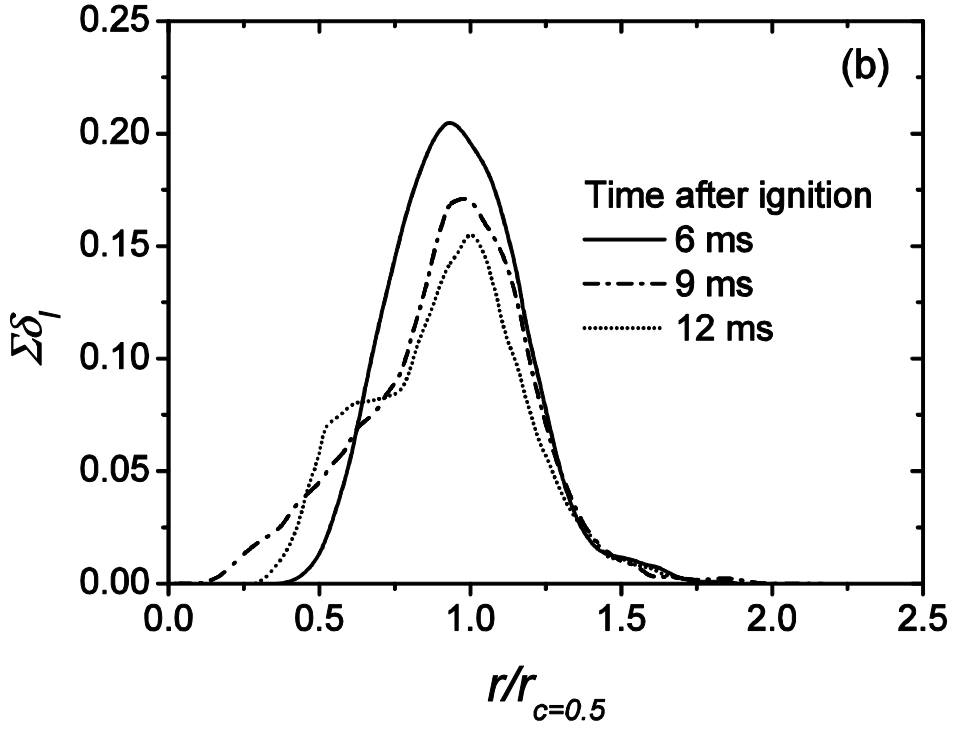

Figure 10. Normalized FSD ($\Sigma\delta_l$) plotted against normalized radius ($r/r_{c=0.5}$) at different time after ignition for methane-air mixture. Figure (a) at ϕ=0.7, u'/u_l =2.35 and (b) at ϕ=1.0, u'/u_l =1.11.

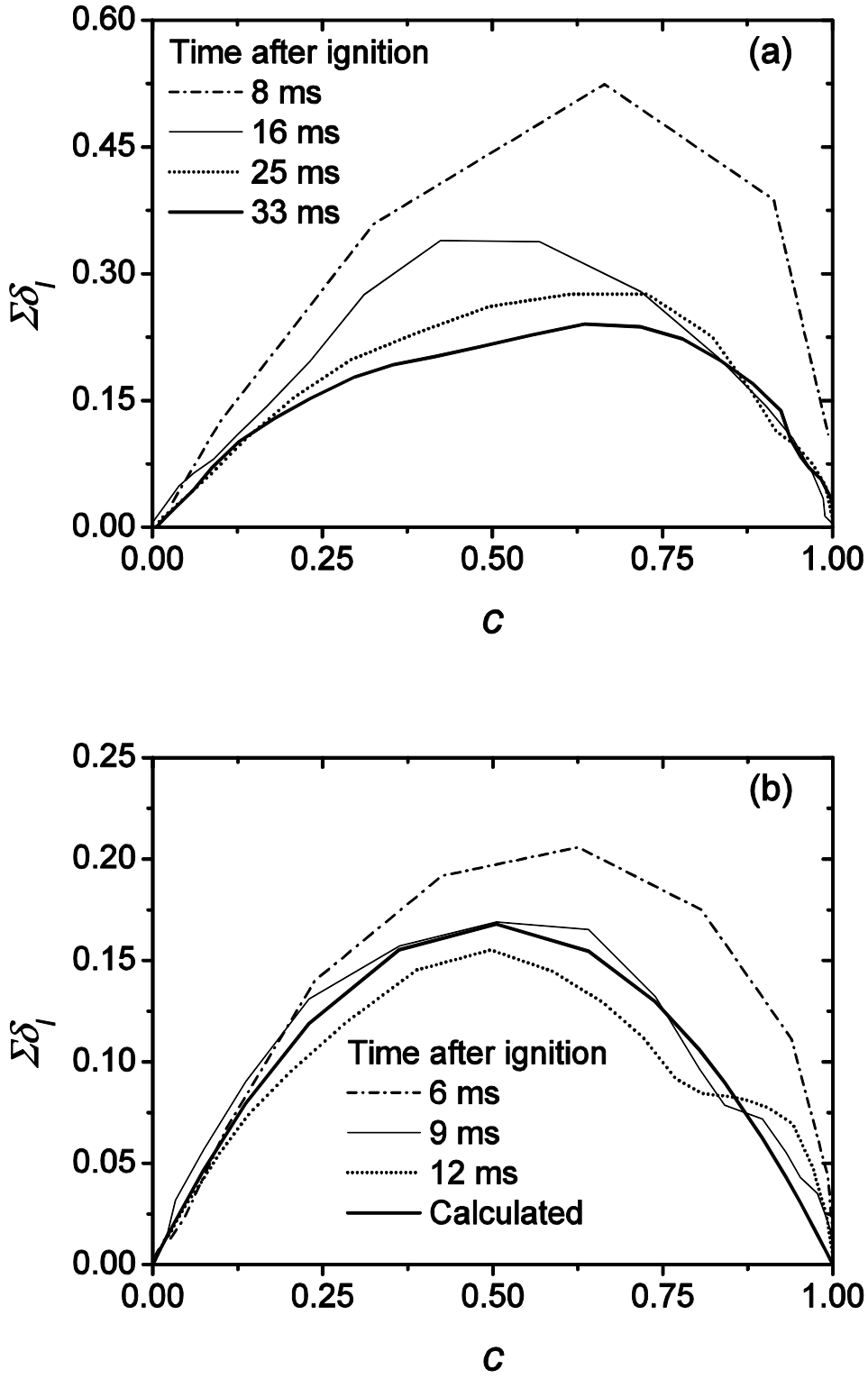

Figure 11. Normalized FSD ($\Sigma\delta_l$) plotted against RPV at different time after ignition for methane-air mixture. Figure (a) at ϕ=0.7, u'/u_l =2.35 and (b) at ϕ=1.0, u'/u_l =1.11. $\Sigma\delta_l$ calculated using Eq. (3) at 9 ms is shown as a thick solid line in Fig. (b).

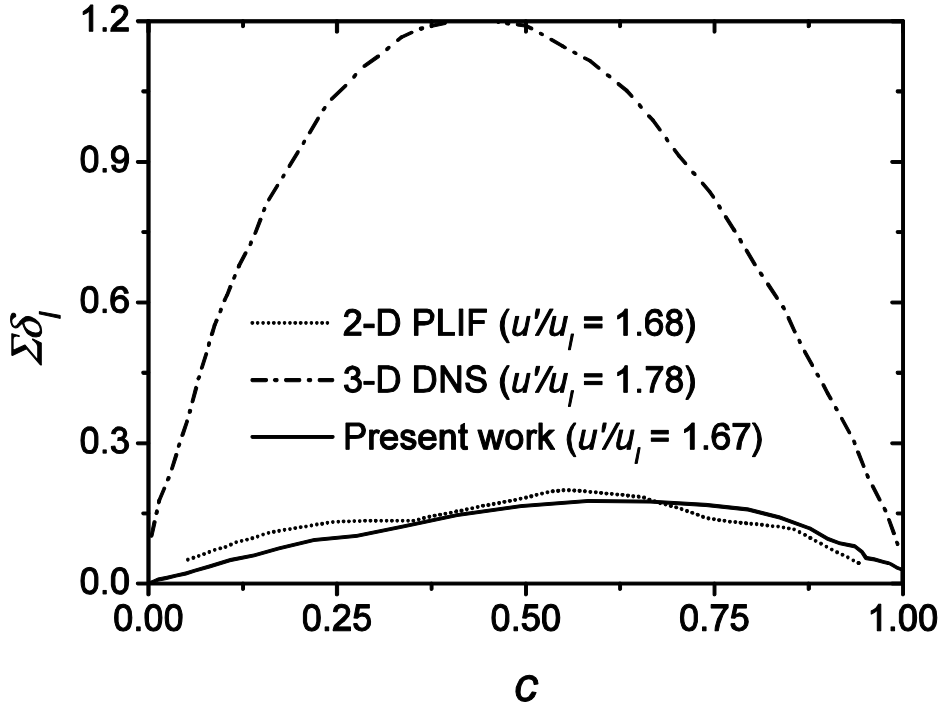

Figure 12. Variation of normalized FSD ($\Sigma\delta_l$) with RPV. Present measurements shown in solid line for methane-air mixture at ϕ=0.8, u'/u_l =1.67. Comparison with 2-D PLIF and 3-D DNS shown in short-dotted and dash-dotted line respectively at comparable u'/u_l . The DNS and PLIF data for methane-air mixture are taken from Hult et al. (2007).